

Geophysical Research Letters[®]



RESEARCH LETTER

10.1029/2024GL110512

Key Points:

- We present InSAR-based, high-resolution maps of 3-D velocities and strain rates in Southern Tibet
- There is prevailing dilatational strain along seven rift zones in Southern Tibet, with a total extension rate of $18.4 \pm 1.7 \text{ mm/yr}$
- We show the distribution and spatial variations of extension rates for seven rift zones

Supporting Information:

Supporting Information may be found in the online version of this article.

Correspondence to:

C. Qu,
dqyquchy@163.com

Citation:

Chen, H., Qu, C., Zhao, D., Shan, X., Li, C., & Dal Zilio, L. (2024). Large-scale extensional strain in Southern Tibet from Sentinel-1 InSAR and GNSS data. *Geophysical Research Letters*, 51, e2024GL110512. <https://doi.org/10.1029/2024GL110512>

Received 4 JUN 2024

Accepted 23 AUG 2024

Author Contributions:

Conceptualization: Chunyan Qu, Dezheng Zhao, Luca Dal Zilio
Data curation: Han Chen
Funding acquisition: Chunyan Qu, Xinjian Shan
Investigation: Han Chen, Chunyan Qu, Dezheng Zhao, Xinjian Shan
Methodology: Dezheng Zhao
Project administration: Chunyan Qu, Xinjian Shan
Resources: Chunyan Qu
Software: Han Chen
Supervision: Chunyan Qu, Xinjian Shan
Validation: Han Chen, Dezheng Zhao
Visualization: Han Chen, Chenglong Li, Luca Dal Zilio
Writing – original draft: Han Chen

© 2024. The Author(s).

This is an open access article under the terms of the [Creative Commons Attribution-NonCommercial-NoDerivs License](#), which permits use and distribution in any medium, provided the original work is properly cited, the use is non-commercial and no modifications or adaptations are made.

Large-Scale Extensional Strain in Southern Tibet From Sentinel-1 InSAR and GNSS Data

Han Chen¹ , Chunyan Qu¹ , Dezheng Zhao² , Xinjian Shan¹ , Chenglong Li¹, and Luca Dal Zilio^{3,4} 

¹State Key Laboratory of Earthquake Dynamics, Institute of Geology, China Earthquake Administration, Beijing, China,

²State Key Laboratory for Mineral Deposits Research, School of Earth Sciences and Engineering, Nanjing University, Nanjing, China, ³Earth Observatory of Singapore, Nanyang Technological University, Nanyang, Singapore, ⁴Asian School of the Environment, Nanyang Technological University, Nanyang, Singapore

Abstract In this study, we utilize C-band Sentinel-1 radar images from 2015 to 2022, combined with interseismic horizontal GNSS velocities, to construct large-scale, high-resolution, 3-D velocity and strain rate maps over a vast region of southern Tibet. We show the distribution of prevailing dilatational strain accumulation along the seven major rift zones. Using 2-D elastic dislocations invoking a two-fault model in a Bayesian framework, we quantified the decadal extension rates across the seven rift zones, and we suggest a total extension rate of $18.4 \pm 1.7 \text{ mm/yr}$, consistent with geological and geodetic estimates. The resulting strain rate maps, combined with the earthquake catalog, help us identify areas with high earthquake potential. Our study enhances our understanding of the present-day tectonics and kinematics in southern Tibet and provides important constraints for seismic hazard assessment in this region.

Plain Language Summary In this research, we used satellite radar images from 2015 to 2022 and GNSS data to study the crustal deformation and strain distribution in southern Tibet, where the Earth's crust is actively stretching due to the collision of the Indian and Eurasian plates and the extrusion of crustal materials. By analyzing high-resolution 3D velocities, we provided new high-resolution surface strain maps over southern Tibet. We found that the widespread dilatational strain is mainly localized along seven major N-S trending rift zones. Seven major rift zones are experiencing extension at a total rate of $18.4 \pm 1.7 \text{ mm/yr}$. The strain rate maps, combined with historical earthquakes, helped us identify fault segments that are more likely to host earthquakes in the future. By mapping deformation and strain in greater detail, we provided valuable data that can improve our understanding of kinematics and earthquake risk assessments in geologically complex southern Tibet.

1. Introduction

The orogenic Tibetan Plateau generates complex crustal deformation due to the ongoing collision between the Indian and Eurasian Plates at a rate of 40–50 mm/yr (Jaeger et al., 1989; Tapponnier & Molnar, 1977; Q. Wang et al., 2001; Dal Zilio et al., 2021). The convergence between the two plates is accommodated by a diverse network of active fault systems, including thrust faulting along and south of the Himalayas and along the Longmenshan, strike-slip faulting along the margins of and within the Tibetan Plateau, and a series of normal faults within the interior of the plateau (Armijo et al., 1986; Yin & Harrison, 2000). These complex fault systems play a crucial role in the geodynamics of the region, but the way and the amount they accommodate plate convergence remain controversial (e.g., Armijo et al., 1986; Molnar & Tapponnier, 1978; Tapponnier et al., 1981).

The present-day crustal deformation around Southern Tibet is suggested to be prominent along seven major N-S trending rift zones: the Yari rift (YRR), Lunggar rift (LGR), Lopu Kangri rift (LKR), Tangra Yum Co rift (TYR), Pumqu-Xainza rift (PXR), Yadong-Gulu rift (YGR), and Cona-Oiga rift (COR). These rifts are generally located between 80°E and 93°E, south of the Bangong-Nujiang Suture (BNS) and north of the Yarlung Zangbo Suture (YZS) (Figure 1a). These rifts are vital for our understanding of the tectonic regime in the region, yet geological studies in this region are still limited due to its remote and elevated terrain (e.g., Kapp & Guynn, 2004; S. Wang et al., 2020; Chevalier et al., 2020). Although Global Navigation Satellite System (GNSS) observations are essential in quantifying the velocity field of southern Tibet, the stations deployed in this region remain sparse and uneven (M. Wang & Shen, 2020). In recent decades, Interferometric Synthetic Aperture Radar (InSAR) has

Writing – review & editing: Han Chen, Chunyan Qu, Dezheng Zhao, Luca Dal Zilio

proven invaluable in imaging crustal deformation across large spatiotemporal scales, revealing unmapped active faults, documenting strain localizations, identifying creeping fault sections, and constraining slip rates and frictional properties (e.g., H. Wang et al., 2009; Jolivet et al., 2013, 2015; Daout et al., 2019; Weiss et al., 2020; Ou et al., 2022; Y. Zhang et al., 2024). Despite significant insights from studies on prominent strike-slip fault systems, such as the Kunlun, Haiyuan, and Xianshuhe faults, knowledge about the kinematics and dynamics of rift systems in southern Tibet remains limited (e.g., H. Wang et al., 2019; Zhao et al., 2022; Z. Huang et al., 2022; Ou et al., 2022; X. Huang et al., 2023; D.-L. Wu et al., 2024).

In this study, we utilized Sentinel-1 imagery spanning 2015–2022 across 12 tracks, 6 ascending tracks and 6 descending tracks, to produce a high-resolution velocity map of southern Tibet. By integrating GNSS data with InSAR, we generated high-resolution 3-D rate maps and derived the strain rate map for southern Tibet using horizontal velocity fields. Our high-resolution observations allowed us to further quantify the present-day extension rates of seven rift zones, enhancing our understanding of regional kinematics and contributing to seismic hazard assessments.

2. Data and Methods

2.1. InSAR Data and Processing

To analyze the present-day surface deformation in Southern Tibet, we utilized C-band SAR data from six ascending and six descending Sentinel-1 tracks (Figures 1b and 1c), spanning from March 2015 to March 2022. Along each track, a single-look complex (SLC) image was chosen as the common reference image, and all SLCs along that track were aligned accordingly. The common reference image was approximately positioned near the center of the temporal-spatial baseline plot (Figure S1 in Supporting Information S1). The co-registered SLCs were then used to generate a stack of interferograms based on the temporal (180–730 days) and spatial (<30 m) baselines using the GAMMA software (Wegmüller & Werner, 1997) to ensure coherence of interferograms. The larger temporal baseline helped maximize the signal-to-noise ratio during InSAR time-series processing (Ansari et al., 2020). We generated a total of 7,677 interferograms, each covering three frames. All interferograms were multilooked with a factor of 100 and 20 in range and azimuth direction, respectively. The topographic phase was removed using the 3-arc-sec Shuttle Radar Topography Mission Digital Elevation Model. The power spectrum method was utilized to spatially filter the random phase noise in interferograms (Goldstein & Werner, 1998). Subsequently, the phase unwrapping was performed using the minimum cost flow (MCF) algorithm (Werner et al., 2000).

We used the Small Baseline Subset (SBAS) method as implemented in the Miami InSAR Time Series Software in Python (Minipy) software to generate the InSAR time series for each track (Y. Zhang et al., 2019). To correct the tropospheric phase delay, we utilized the Generic Atmospheric Correction Online Service (GACOS) model (Yu et al., 2018). Figure 1d shows a comparison of an interferogram before (blue dots) and after (orange dots) atmospheric delay corrections using GACOS, notably mitigating noise that was linearly related to the elevation. The residual long-wavelength (orbital) error was removed by fitting a planar ramp from each interferogram, and we calculated a correction term for each epoch through a network correction (e.g., Biggs et al., 2007; Maubant et al., 2020; Ou et al., 2022). The stack of corrected interferograms along each track was then used to calculate a mean velocity field over the observation period (Figures 1b and 1c).

2.2. GNSS Data

In this study, we used interseismic horizontal GNSS velocities from M. Wang and Shen (2020). Vertical GNSS velocities in this region were published in Liang et al. (2013). However, considering the relatively few GNSS stations with reliable vertical velocities compared to the horizontal ones (see Figure S2 in Supporting Information S1 for a comparison of the sites available for GNSS vertical and horizontal velocities), we subsequently utilized only the horizontal velocities in our analysis.

2.3. InSAR LOS Velocity Decomposition

Before decomposing the Line of Sight (LOS) velocities, we validated the accuracy of InSAR LOS velocities by checking the consistency of velocities at the same location in overlapping regions between adjacent tracks. Figure 1e illustrates the velocity discrepancies. The mean and standard deviation (STD) of velocity differences for

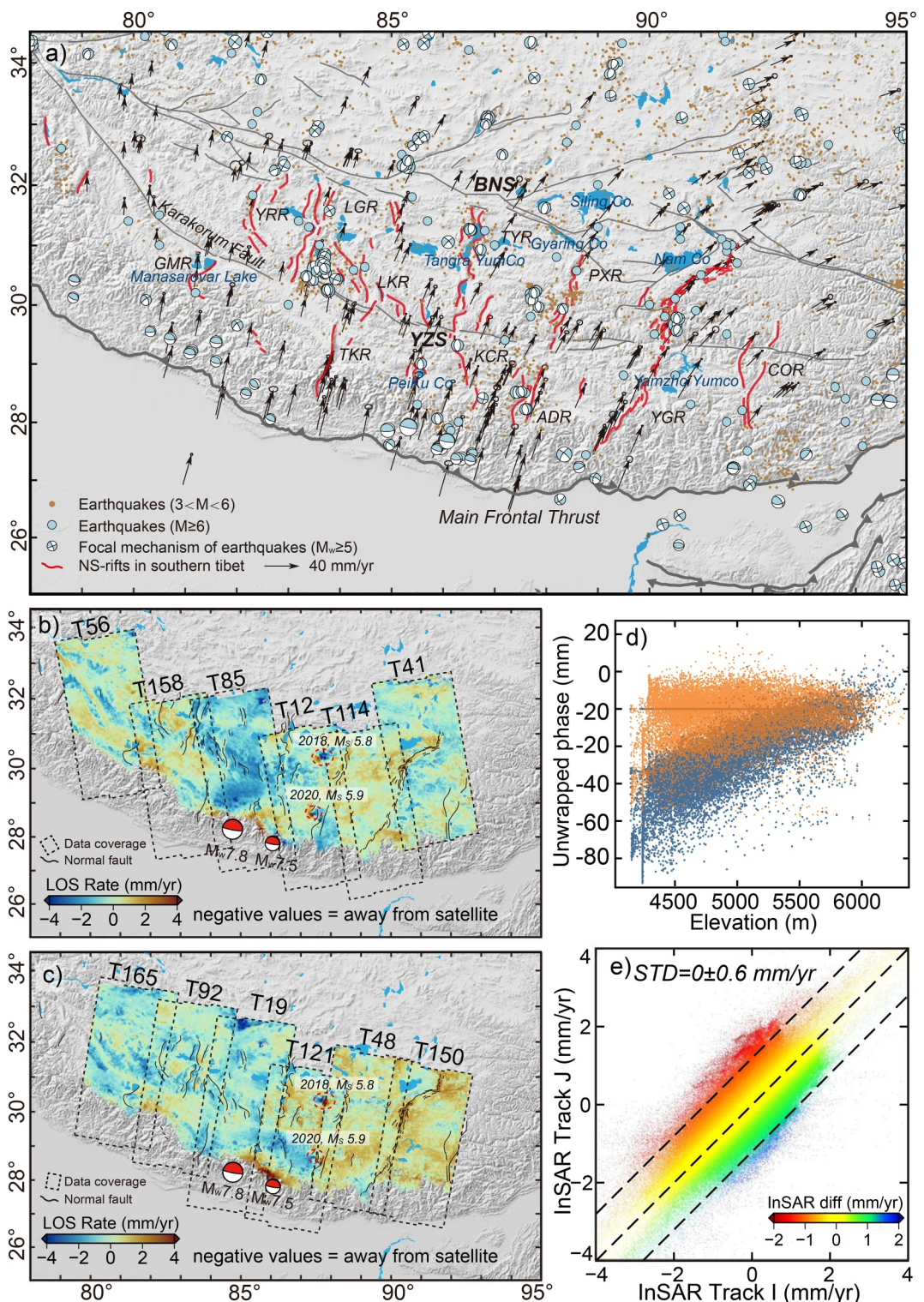


Figure 1. (a) Topography, active faults, seismicities, and interseismic GNSS velocities within southern Tibet. Red lines represent rifts, and gray lines represent active faults, compiled from Deng (2003), K. Li et al. (2022) and K. Li et al. (2023). Epicenters (brown dots, before 2020) are from the China Earthquake Networks Center. Focal mechanisms are from the GCMT catalog. Horizontal GNSS velocities (gray arrows) in the Eurasia-fixed reference frame are from M. Wang and Shen (2020). GMR, Gurla Mandhata rift; TKR, Thakkola rift; KCR, Kung Co rift; ADR, Ama Drime rift (b, c) Line-of-sight (LOS) InSAR rate maps from ascending and descending tracks, respectively. (d) Scatterplot showing the distribution of unwrapped phase of the interferogram as a linear function of elevation before atmospheric delay corrections (blue dots). Orange dots show post-atmospheric delay corrections. (e) Scatterplot showing InSAR LOS rate discrepancies in overlapping regions of adjacent tracks along all ascending and descending tracks. Dashed lines show 2σ bounds of the differences.

all tracks were 0 and 0.6 mm/yr, respectively. These discrepancies stemmed partly from variations in the incidence angle along different tracks and partly from residual noise in the velocity measurements. Overall, the small discrepancy indicated the robustness of our LOS rate maps.

The mean InSAR LOS velocity for each track was referenced independently in a local reference frame during phase unwrapping of interferograms (Figures 1b and 1c). To align all velocity maps along ascending and descending tracks in the same reference frame, we employed a second-order polynomial fitting to transform the InSAR LOS velocities using GNSS LOS-converted velocities, taking the local incidence angle of each pixel into consideration (Hussain et al., 2018). Here, we did not consider the vertical GNSS velocities, because the vertical velocities were rather sparse, hindering a reliable interpolation. The transformation of the InSAR reference frame here would align long-wavelength signals with GNSS observations but retained the local short-wavelength features (e.g., Weiss et al., 2020). We interpolated northward velocities of interseismic GNSS data, using the method proposed by Shen et al. (2015) (Figure S3 in Supporting Information S1). We then combined the interpolated GNSS northward velocities (V_N) with ascending and descending InSAR LOS velocities in the Eurasia-fixed reference frame (Figure S4 in Supporting Information S1) to calculate the E-W (V_E) and vertical velocity (V_U) components, following the approach of Hussain et al. (2018) and Weiss et al. (2020) (Text S1 in Supporting Information S1).

3. 3-D Velocities and Strain Rates

During our InSAR observation period, two large earthquakes occurred: the 2018 Ms 5.8 Xietongmen earthquake and the 2020 Ms 5.9 Dingri earthquake (Figures 1b and 1c). We masked out the regions affected by these earthquakes in our tectonic analysis.

The decomposed vertical velocity field was dominated by localized, short-wavelength signals, which were not spatially correlated with faults and active tectonics and were thought to be related to hydrology, permafrost, or anthropogenic activities (Wright et al., 2023). The postseismic deformation in the aftermath of the 2015 Mw7.8 Gorkha earthquake was captured by our observations. Near the source region of the 2015 Gorkha earthquake, we observed uplift rates of up to 7 mm/yr, which is spatially correlated to the down-dip afterslip north of Kathmandu (green dashed ellipse in Figure 2b), as well as subsidence (~ 1 mm/y) further to the north (red dashed ellipse in Figure 2b) that was attributed to viscoelastic relaxation in the lower crust beneath the Tibetan Plateau (K. Wang & Fialko, 2018; Hong & Liu, 2021). In contrast, the V_E map primarily exhibited long-wavelength deformation (Figures 2a and 2g). The E-W velocity along the profile LL', consistent with GNSS E-W velocities, showed an overall increase from 1 mm/yr in the west (80.0°E) to 18 mm/yr in the east (92.2°E), indicating lateral crustal extension in south Tibet (Figure 2g).

Before the calculation of the strain rate, the V_E map was downsampled to a grid size of 1 km in order to reduce the computational load. To reduce the random phase noise in the V_E map, we applied a sliding median filter (using grdfilter in GMT software) to the V_E results (Figure S4 in Supporting Information S1). The window size of the filter was 60×60 km, similar to Ou et al. (2022), which could effectively smooth the data without losing important short-wavelength signals. We then calculated the horizontal dilatational strain rates following the approach developed by Ou et al. (2022). The horizontal strain-rate tensor ϵ can be represented as a 2-dimension matrix using the gradients $\partial V_E / \partial x$, $\partial V_E / \partial y$, $\partial V_N / \partial x$, $\partial V_N / \partial y$, so that the infinitesimal dilatational strain rate (ϵ_{dil}), and the second invariant of the horizontal strain-rate tensor (ϵ_2) were defined as follows (Ou et al., 2022; Sandwell & Wessel, 2016):

$$\epsilon = \begin{bmatrix} \epsilon_{xx} & \epsilon_{xy} \\ \epsilon_{yx} & \epsilon_{yy} \end{bmatrix} = \begin{bmatrix} \frac{\partial V_E}{\partial x} & \frac{1}{2} \left(\frac{\partial V_E}{\partial y} + \frac{\partial V_N}{\partial x} \right) \\ \frac{1}{2} \left(\frac{\partial V_N}{\partial x} + \frac{\partial V_E}{\partial y} \right) & \frac{\partial V_N}{\partial y} \end{bmatrix} \quad (1)$$

$$\epsilon_{dil} = \epsilon_{xx} + \epsilon_{yy} \quad (2)$$

$$\epsilon_2 = \sqrt{\epsilon_{xx}^2 + 2\epsilon_{xy}^2 + \epsilon_{yy}^2} \quad (3)$$

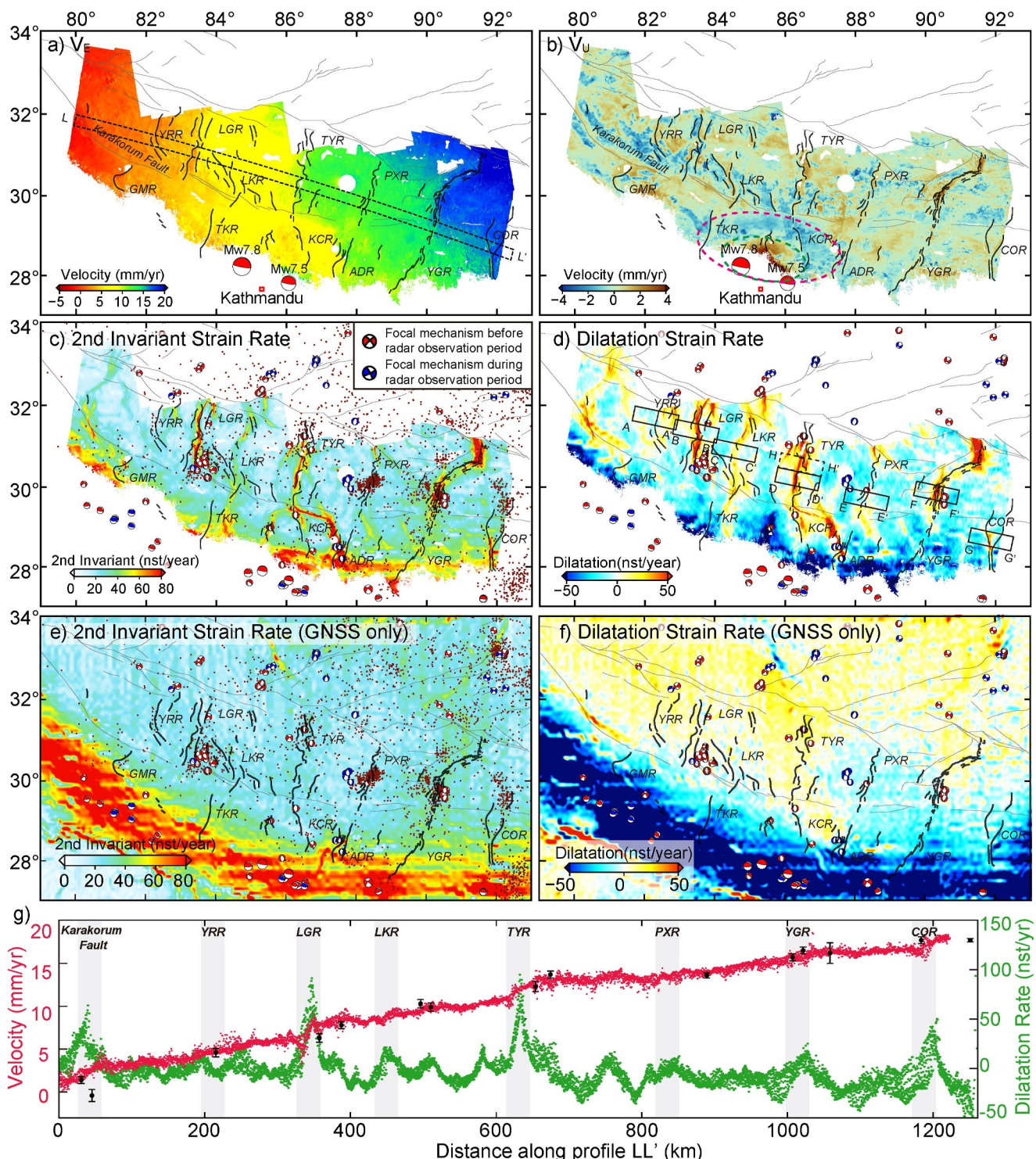


Figure 2. 3-D velocity and horizontal strain rates derived from GNSS and InSAR jointly or separately (a, b) E-W, and vertical velocities. (c) Second invariant strain rate and (d) dilatational strain rate calculated from the interpolated GNSS V_N and InSAR-derived V_E . (e) Second invariant and (f) dilatational strain rate calculated from the interpolated GNSS V_N and V_E . Brown dots in (c, e) indicate historical earthquakes (before 2020). (g) Red dots show InSAR-derived E-W velocities along profile LL' (see location in a). Green dots show the dilatation rate along profile LL'. Black dots indicate the E-W GNSS velocities with 1σ uncertainties (M. Wang & Shen, 2020). Gray bars indicate the locations of the major fault and rifts.

Overall, localized, short-wavelength signals can be better resolved in the high-resolution InSAR-based strain rate fields (Figures 2c and 2d) than GNSS-based strain rate maps (Figures 2e and 2f). GNSS-based strain rate maps showed the highest contractional strain rates along the Himalayan arc, reflecting the rapid accumulation of convergence strain along the convergence zone between the India-Eurasia plates (M. Wang & Shen, 2020). In contrast, our InSAR-based, high-resolution strain maps clearly showed prevailing high, localized dilatational strain rates along major rift zones, which were not well documented by previous studies due to the limited density of GNSS observations (H. Wang et al., 2019; M. Wang & Shen, 2020). We suggested that all seven rift zones were undergoing significant extension, among which the dilatational strain rate along the LGR, the TYR, the YGR, and the COR, had values of >50 nanostrain/yr (Figures 2d and 2g).

The second invariant of the strain rate tensor, which measures the magnitude of the total strain, showed a similar pattern to our dilatational strain rate maps (Figure 2c). Our high-resolution strain rate maps helped to better identify the rate of strain accumulation in south Tibet. By comparing with the historical earthquake catalog, we suggested a spatial correlation between zones of high second invariant strain rates and the clustered historical earthquakes (Figure 2c). We found that the northern YGR showed high strain rates but with limited instrumental historical earthquakes and no geodetic evidence of creeping, suggesting a high earthquake potential there.

Despite many historical earthquakes that occurred along the PXR, most segments of the PXR showed low dilatation strain rates (Figures 3c and 3d), consistent with H. Wang et al. (2019). However, the influence of coseismic effects from neighboring areas cannot be excluded. The area enclosed by the TKR, the ADR, and the YZS exhibited a high dilatation strain rate, which may have been related to the post-seismic deformation of the Gorkha earthquake.

4. Extension Rates of Seven Rift Zones in Southern Tibet

Ascending and descending LOS velocities across the rift zones offered constraints on strain localization and fault slip rates. We extracted one fault-perpendicular velocity swath (40 km wide and 120 km long) across each of the seven rifts from ascending and descending InSAR LOS velocities (see example in Figure 3a). The locations of the seven velocity swaths were illustrated in Figure 2d. We utilized a simple 2-D elastic dislocation model (Segall, 2010; Z. Huang et al., 2022) to estimate kinematic parameters, including fault slip rates (strike-slip and dip-slip), dip angles, locking depths, and fault locations (see details in Text S2 in Supporting Information S1). We used a Bayesian algorithm with a Markov Chain Monte Carlo (MCMC) sampler to estimate the PDF of the parameters (Goodman & Weare, 2010). We used a uniform distribution for all priors within certain bounds, inspired by geological slip rates, geodetic data, and the mapped fault geometry (Armijo et al., 1986; H. Wang et al., 2019; Chevalier et al., 2020; S. Wang et al., 2022). We ran a total of 10,000,000 iterations for each inversion, discarding the first 40% of iterations as burn-in, and computed the posterior mean and standard deviation values for the model parameters to represent an ensemble solution and the corresponding uncertainties (Figure 3c).

We found that the deformation across each of the rift zones was partitioned into two faults rather than being localized on a single fault. That was supported by the fact that the model invoking only a single fault failed to fit the ascending and descending observations well simultaneously, especially the near-field observations (Figure S5a in Supporting Information S1). Tectonic observations and models showed that the rift zones were often composed of a complex array of closely spaced, subparallel faults, which was also clear in tectonic traces of multiple faults in the single rift zone (Figure S5b in Supporting Information S1) (Armijo et al., 1986; Chevalier et al., 2020). These faults jointly played a role in absorbing regional extension, potentially explaining why single-fault models failed to match the data. We, therefore, revised the single-fault model, invoking two boundary faults to fit the ascending and descending LOS observations (Figures 3a and 3b, Figure S6 in Supporting Information S1). Geodetic observations alone did not permit the discrimination of three faults or more.

The probability density functions (PDFs) shown in Figures S7-S13 in Supporting Information S1 illustrated the trade-off between dip-slip rates and locking depths, which was common in similar 2D inversions (e.g., Hussain et al., 2018; Z. Huang et al., 2022). Additionally, we observed a trade-off between the dip-slip rates of two boundary faults. In the subsequent analysis, we only focused on the total slip rates of the two boundary faults across each rift zone. Due to the sensitivity of InSAR observations to the E-W extension motion and the nearly north-south trend of rifts, dip-slip was better constrained than the strike-slip. Since these rift zones primarily exhibited

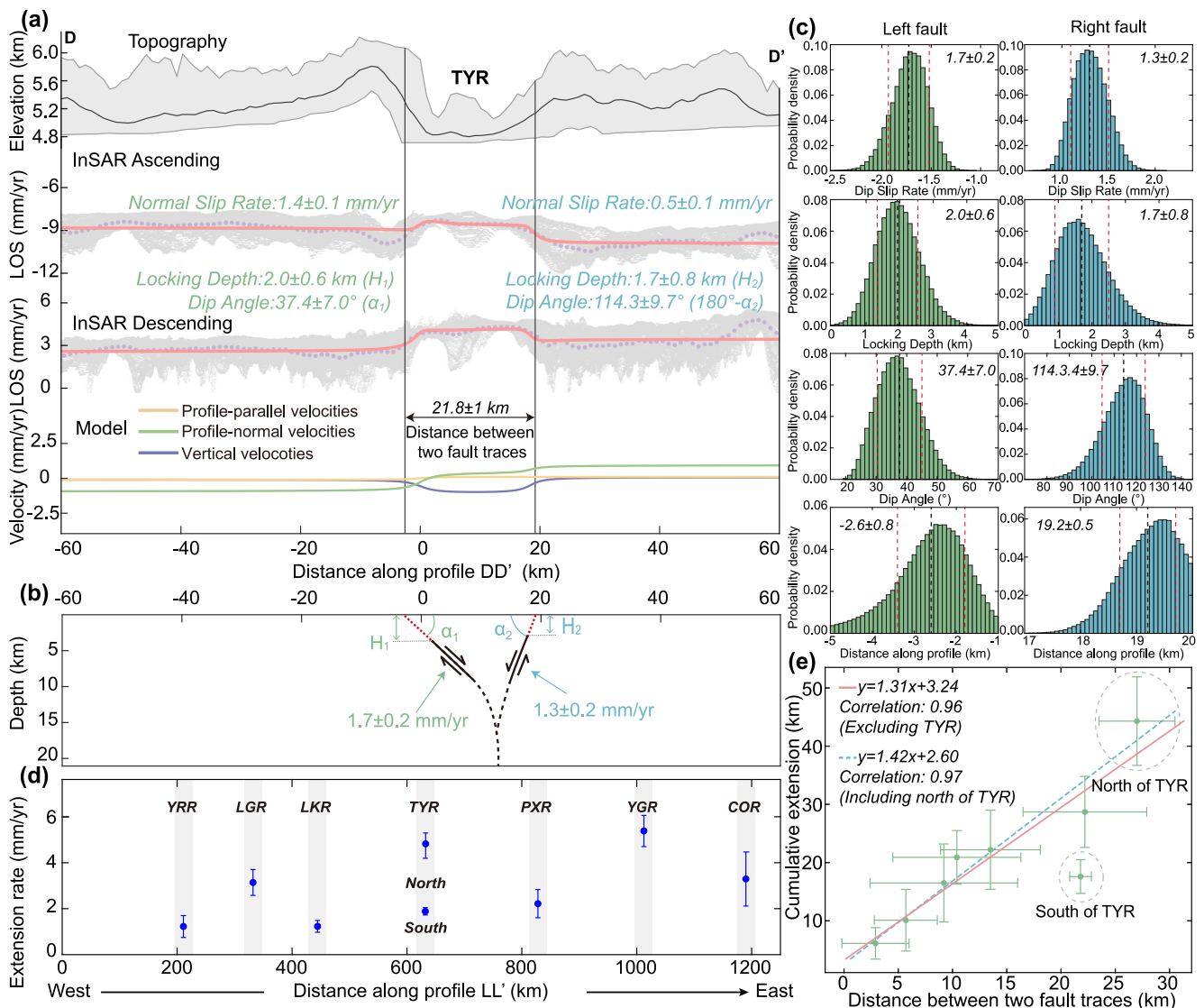


Figure 3. Inversion results for the TYR and extension slip rates across seven rift zones. (a) Top: profile DD' topography (average elevation: black line; min/max: gray lines). Middle: InSAR LOS velocities (gray points; mean over 1 km bins: light purple) with predicted velocities (red line). Bottom: model-predicted fault-parallel, fault-normal, and vertical velocities. (b) 2-D fault geometry in the two-fault model (freely slipping part: black lines; locked part: red dashed lines). (c) Posterior marginal PDFs for model parameters across the TYR. Numbers indicate best-fitting parameters. (d) Total extension rates of boundary faults across each rift zone. (e) Cumulative extension versus distance between boundary faults.

dip-slip motion with minimal strike-slip motion (Armijo et al., 1986; Chevalier et al., 2020), the poorly resolved strike-slip rates were unlikely to substantially bias our subsequent analyses of extension rates of the rift zones.

The faster extension rates are observed in the LGR, the TYR, the COR, and the YGR, with values of 3.1 ± 0.6 mm/yr, 1.9 ± 0.2 mm/yr, 3.3 ± 1.2 mm/yr, and 5.4 ± 0.7 mm/yr, respectively, corresponding to the high dilatational strain rates. In contrast, the YRR and the LKR exhibit lower extension rates of 1.2 ± 0.5 mm/yr and 1.2 ± 0.3 mm/yr, respectively. Although the dilatational strain rate of the PXR is lower than that of the TYR, its extension rate is close to the TYR, 2.2 ± 0.6 mm/yr. The relatively shallow locking depth of the TYR (~ 2 km) appears to account for the close extension rates but large extension strain rate differences.

Rift development can generally be divided into three stages: initial stage (extension initiation), stretching stage (extension acceleration), and final subsidence stage (extension halt) (Fossen, 2016). The extension rate during the initial stage was inferred to be one-third of that during the stretching stage in LGR (Styron et al., 2013). We assumed a constant rate during each stage and similar to the LGR, the extension rate in initial stage is also

one-third of stretching stage. Note that the extension rate estimated in this study reflected the present-day stage (i.e., stretching stage). We then summarized the timing of extension initiation and acceleration for each rift (see Table S1, Armijo et al., 1986; Harrison et al., 1995; Kapp et al., 2005; Dewane et al., 2006; Zhong-hai et al., 2007; Kapp et al., 2008; Hager et al., 2009; Murphy et al., 2010; Woodruff Jr et al., 2013; Sundell et al., 2013; Sanchez et al., 2013; Wolff et al., 2023). Based on these assumptions, we calculated the total extension for each rift zone since its initiation (details in Text S3 in Supporting Information S1). We found that, except for the TYR, there was a strong correlation between the estimated distance between two boundary faults in our model and the calculated cumulative extension (Figure 3e). In the north TYR, we tested another profile (HH'), and the inversion results from this profile were also consistent with this linear relationship (Figure 3e). The observation that the total extension of the south TYR is less than the distance between its two fault traces suggested that the south TYR may have gradually switched from stretching stage to final subsidence stage, with the current extension rate being lower than that observed in its stretching stage.

5. Discussion and Conclusions

Our study presented a comprehensive analysis of crustal deformation and strain distribution in southern Tibet using Sentinel-1 InSAR data combined with GNSS observations. The high-resolution 3-D velocity and strain rate maps revealed significant insights into the tectonic activity along seven major N-S rift zones. One of the main findings of this study was the high dilatational strain rates along the LGR, TYR, YGR, and COR with values exceeding 50 nanostrain/yr. These strain rates are higher than previously documented due to the limited density of GNSS observations (H. Wang et al., 2019; M. Wang & Shen, 2020). Our results highlighted the importance of using high-resolution InSAR data to capture localized strain rates that are crucial for understanding regional kinematics and seismic hazard assessments.

Our study identified areas with high earthquake potential by correlating strain rate maps with historical earthquake data (Figure 2c). The northern part of the YGR, despite showing high strain rates, had limited historical seismic activity, indicating a high potential for future earthquakes. The COR showed high strain rates and was another area of concern for future seismic activity. In contrast, the PXR, despite experiencing several historical earthquakes, showed lower dilatational strain rates in most segments. This could have indicated a currently lower risk of seismic activity compared to other rifts, although the influence of coseismic effects from neighboring areas could not be excluded. The YRR and LKR rifts also displayed lower extension and strain rates, implying a lower immediate seismic hazard, but these areas should still be monitored due to the potential for significant seismic events given the regional tectonic context. Furthermore, the ADR and the TKR, which showed high strain rates correspond to two regions where the interseismic coupling of the Main Himalayan Thrust (MHT) had been previously inferred to indicate low coupling (Dal Zilio et al., 2020). These potential barriers of low coupling suggested a structural segmentation of the MHT imposed by inherited tectonic structures from the India-Eurasia collision.

We found that these rifts were experiencing a total extension rate of 18.4 ± 1.7 mm/yr (Figure 4), consistent with geodetic estimates (Q. Wang et al., 2001; P.-Z. Zhang et al., 2004; H. Wang et al., 2019). Our geodetic estimate exceeded the geological rates of 10 ± 5.6 mm/yr and 9 ± 2 mm/yr (Armijo et al., 1986; Chevalier et al., 2020), which were derived by assuming comparable extension rates across seven rift zones, specifically by multiplying the YGR extension rates (1.4 ± 0.8 mm/yr and 1.3 ± 0.3 mm/yr) by 7. However, our findings showed clear spatial variations in extension rates, which were more accurately captured by our high-resolution InSAR and GNSS data integration (H. Wang et al., 2019). Additionally, variations in extension rates along the same rift contributed to the differences. The YGR, the longest rift in southern Tibet, had a long-term extension rate of ~ 1 mm/yr south of Damxung and increasing to 3–6 mm/yr north of Damxung (Figure 4) (Zhonghai et al., 2004; Z. Wu et al., 2015; Ha et al., 2019; S. Wang et al., 2020; Chevalier et al., 2020). Present-day GNSS data constrained the decadal extension rate of the YGR, ranging from 2 ± 0.6 mm/yr to 9.3 ± 2.2 mm/yr, likely due to varying model hypotheses in geodetic studies (e.g., rigid or internally deforming blocks, different numbers of blocks and boundary locations, and distinct constraints on fault locking depths) (Q. Chen, Freymueller, Yang, et al., 2004; Q. Chen, Freymueller, Wang, et al., 2004; Gan et al., 2007; W. Wang et al., 2017; Tian et al., 2019).

We inverted extension rates along the YGR using InSAR observations from a 20 km wide and 120 km long swath (Figures S14, S15 in Supporting Information S1). The first-order trend, where extension rates were lower in the south and higher in the north, was consistent with geological observations (Figure 4), whereas Tian et al. (2019)

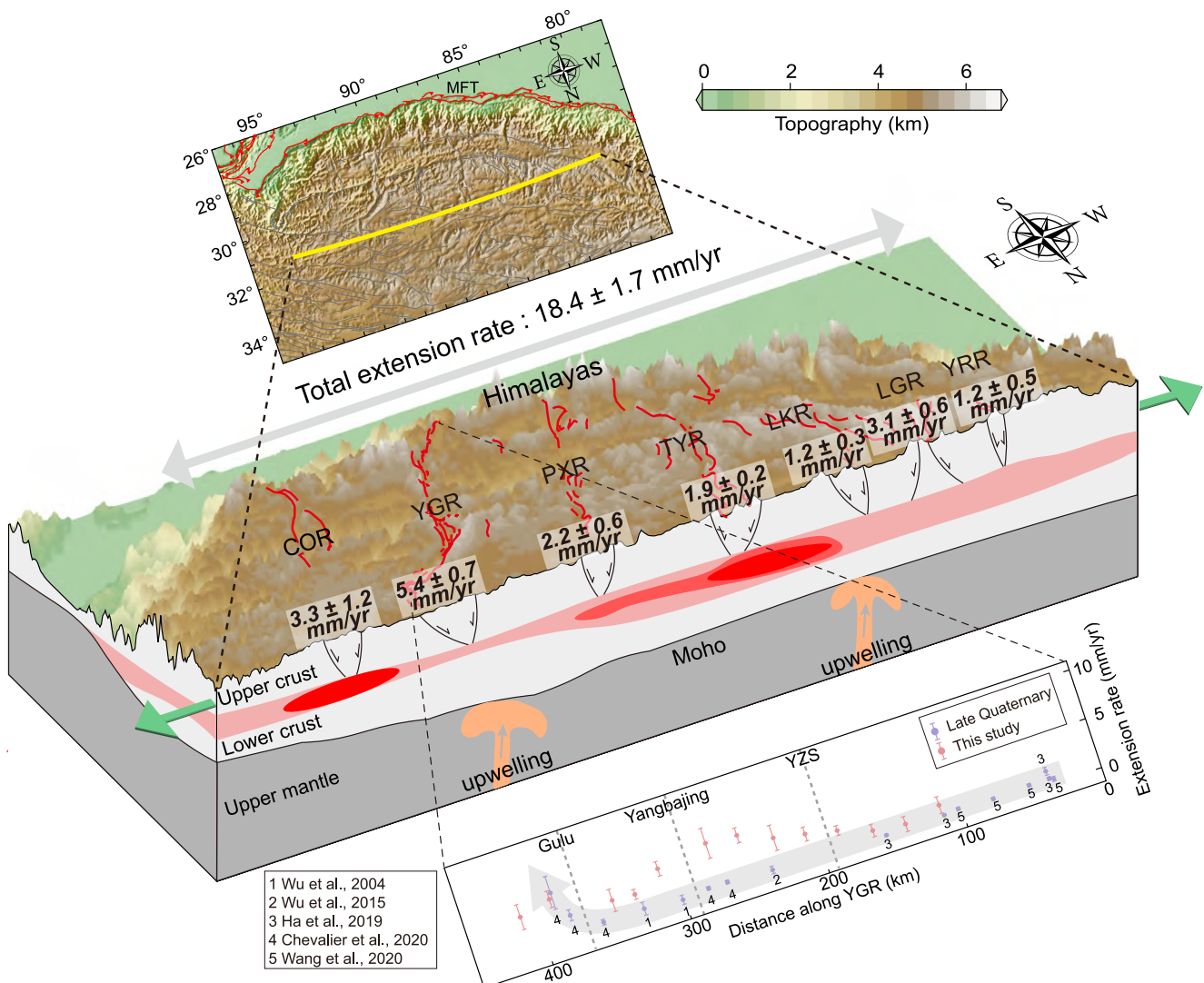


Figure 4. Schematic of the seven rift zones in the upper crust of southern Tibet, plotted with reference to Pang et al. (2022). The red lines denote the N–S rifts, the black lines on the profile indicate the two boundary faults of these rifts as determined from our inversionn. The red zones represent weak crustal zones (S. Huang et al., 2020). Two yellow upwelling zones represent the small-scale asthenospheric upwelling (J. Li & Song, 2018).

observed an opposite trend with higher rates in the south (8 ± 0.9 mm/yr) and lower in the north (5.6 ± 0.8 mm/yr). The reduction in extension rates from Yangbajing to the Gulu Bend may have been due to substantial changes in fault strike, shifting from extension to strike-slip motion. Our results were notably higher than the geological extension rates between YZS and Gulu, possibly because our analysis included all distributed deformation in the area, not just the primary rift.

In conclusion, our high-resolution strain rate maps provided valuable data for understanding the present-day kinematics of southern Tibet. The integration of InSAR and GNSS data allowed for a detailed assessment of extension rates and strain distribution, offering new insights into the tectonic processes and seismic hazards in this region. The total extension rate of 18.4 ± 1.7 mm/yr across seven rift zones enhanced our understanding of the regional tectonic regime and provided important constraints for future seismic hazard assessments.

Data Availability Statement

The ascending and descending InSAR LOS velocity, and the strain rate fields that we derived are available at Zenodo archive via H. Chen et al. (2024).

Acknowledgments

The authors thank the Editor Fabio Capitanio, Jeff Freymueller, the Associate Editor, and an anonymous reviewer for their constructive reviews. This work was supported by the National Natural Science Foundation of China (42374007, 42174009), the Basic Scientific Funding of Institute of Geology, China Earthquake Administration (IGCEA2104). L. Dal Zilio was supported by the European Research Council (ERC) Synergy Grant "Fault Activation and Earthquake Rupture" (FEAR) (856559), the Earth Observatory of Singapore (EOS), and the Singapore Ministry of Education Tier 3b project "Investigating Volcano and Earthquake Science and Technology (InVEST)" (Award MOE-MOET32021-0002).

References

- Ansari, H., De Zan, F., & Parizzi, A. (2020). Study of systematic bias in measuring surface deformation with sar interferometry. *IEEE Transactions on Geoscience and Remote Sensing*, 59(2), 1285–1301. <https://doi.org/10.1109/tgrs.2020.3003421>
- Armijo, R., Tapponnier, P., Mercier, J., & Han, T.-L. (1986). Quaternary extension in southern tibet: Field observations and tectonic implications. *Journal of Geophysical Research*, 91(B14), 13803–13872. <https://doi.org/10.1029/jb091ib14p13803>
- Biggs, J., Wright, T., Lu, Z., & Parsons, B. (2007). Multi-interferogram method for measuring interseismic deformation: Denali fault, Alaska. *Geophysical Journal International*, 170(3), 1165–1179. <https://doi.org/10.1111/j.1365-246x.2007.03415.x>
- Chen, H., Qu, C., Zhao, D., Shan, X., Li, C., & Dal Zilio, L. (2024). Velocity and strain rate fields of the Southern Tibetan Plateau. *Zenodo*. Retrieved from <https://doi.org/10.5281/zenodo.1332511>
- Chen, Q., Freymueller, J. T., Wang, Q., Yang, Z., Xu, C., & Liu, J. (2004). A deforming block model for the present-day tectonics of tibet. *Journal of Geophysical Research*, 109(B1). <https://doi.org/10.1029/2002jb002151>
- Chen, Q., Freymueller, J. T., Yang, Z., Xu, C., Jiang, W., Wang, Q., & Liu, J. (2004). Spatially variable extension in southern tibet based on gps measurements. *Journal of Geophysical Research*, 109(B9). <https://doi.org/10.1029/2002jb002350>
- Chevalier, M.-L., Tapponnier, P., van Der Woerd, J., Leloup, P. H., Wang, S., Pan, J., et al. (2020). Late quaternary extension rates across the northern half of the yadong-gulu rift: Implication for east-west extension in southern tibet. *Journal of Geophysical Research: Solid Earth*, 125(7), e2019JB019106. <https://doi.org/10.1029/2019jb019106>
- Dal Zilio, L., Hetényi, G., Hubbard, J., & Bollinger, L. (2021). Building the himalaya from tectonic to earthquake scales. *Nature Reviews Earth and Environment*, 2(4), 251–268. <https://doi.org/10.1038/s43017-021-00143-1>
- Dal Zilio, L., Jolivet, R., & van Dinther, Y. (2020). Segmentation of the main himalayan thrust illuminated by bayesian inference of interseismic coupling. *Geophysical Research Letters*, 47(4), e2019GL086424. <https://doi.org/10.1029/2019gl086424>
- Daout, S., Sudhaus, H., Kausch, T., Steinberg, A., & Dini, B. (2019). Interseismic and postseismic shallow creep of the north qaidam thrust faults detected with a multitemporal insar analysis. *Journal of Geophysical Research: Solid Earth*, 124(7), 7259–7279. <https://doi.org/10.1029/2019jb017692>
- Deng, Q.-d. (2003). Active tectonics and earthquake activities in China (in Chinese). *Earth Science Frontiers*, 10(1), 66.
- Dewane, T., Stockli, D., Hager, C., Taylor, M., Ding, L., Lee, J., & Wallis, S. (2006). Timing of cenozoic ew extension in the tangra yum co-kung co rift, south-central tibet. *Agu Fall Meeting Abstracts*, 2006, T34C-04.
- Fossen, H. (2016). *Structural geology*. Cambridge university press.
- Gan, W., Zhang, P., Shen, Z.-K., Niu, Z., Wang, M., Wan, Y., et al. (2007). Present-day crustal motion within the Tibetan plateau inferred from gps measurements. *Journal of Geophysical Research*, 112(B8). <https://doi.org/10.1029/2005jb004120>
- Goldstein, R. M., & Werner, C. L. (1998). Radar interferogram filtering for geophysical applications. *Geophysical Research Letters*, 25(21), 4035–4038. <https://doi.org/10.1029/1998gl900033>
- Goodman, J., & Weare, J. (2010). Ensemble samplers with affine invariance. *Communications in Applied Mathematics and Computational Science*, 5(1), 65–80. <https://doi.org/10.2140/camcos.2010.5.65>
- Ha, G., Wu, Z., & Liu, F. (2019). Late quaternary vertical slip rates along the southern yadong–gulu rift, southern Tibetan plateau. *Tectonophysics*, 755, 75–90. <https://doi.org/10.1016/j.tecto.2019.02.014>
- Hager, C., Stockli, D., Dewane, T., Gehrels, G., & Ding, L. (2009). Anatomy and crustal evolution of the central lhasa terrane (s-tibet) revealed by investigations in the xainza rift. In *Egu general assembly conference abstracts*.11346
- Harrison, T. M., Copeland, P., Kidd, W., & Lovera, O. M. (1995). Activation of the nyainqntanglha shear zone: Implications for uplift of the southern Tibetan plateau. *Tectonics*, 14(3), 658–676. <https://doi.org/10.1029/95tc00608>
- Hong, S., & Liu, M. (2021). Postseismic deformation and afterslip evolution of the 2015 gorkha earthquake constrained by insar and gps observations. *Journal of Geophysical Research: Solid Earth*, 126(7), e2020JB020230. <https://doi.org/10.1029/2020jb020230>
- Huang, S., Yao, H., Lu, Z., Tian, X., Zheng, Y., Wang, R., et al. (2020). High-resolution 3-d shear wave velocity model of the Tibetan plateau: Implications for crustal deformation and porphyry cu deposit formation. *Journal of Geophysical Research: Solid Earth*, 125(7), e2019JB019215. <https://doi.org/10.1029/2019jb019215>
- Huang, X., Li, Y., Shan, X., Zhao, D., Gao, Z., Gong, W., & Qu, C. (2023). Insar observations reveal variations in shallow creep on the kangding segment of the xianshuuhe fault. *Seismological Research Letters*, 94(5), 2291–2300. <https://doi.org/10.1785/0220230053>
- Huang, Z., Zhou, Y., Qiao, X., Zhang, P., & Cheng, X. (2022). Kinematics of the 1000 km haiyuan fault system in northeastern tibet from high-resolution sentinel-1 insar velocities: Fault architecture, slip rates, and partitioning. *Earth and Planetary Science Letters*, 583, 117450. <https://doi.org/10.1016/j.epsl.2022.117450>
- Hussain, E., Wright, T. J., Walters, R. J., Bekaert, D. P., Lloyd, R., & Hooper, A. (2018). Constant strain accumulation rate between major earthquakes on the north anatolian fault. *Nature Communications*, 9(1), 1392. <https://doi.org/10.1038/s41467-018-03739-2>
- Jaeger, J.-J., Courtillot, V., & Tapponnier, P. (1989). Paleontological view of the ages of the deccan traps, the cretaceous/tertiary boundary, and the India-asia collision. *Geology*, 17(4), 316–319. [https://doi.org/10.1130/0091-7613\(1989\)017<0316:pvtao>2.3.co;2](https://doi.org/10.1130/0091-7613(1989)017<0316:pvtao>2.3.co;2)
- Jolivet, R., Candela, T., Lasserre, C., Renard, F., Klinger, Y., & Doin, M.-P. (2015). The burst-like behavior of aseismic slip on a rough fault: The creeping section of the haiyuan fault, China. *Bulletin of the Seismological Society of America*, 105(1), 480–488. <https://doi.org/10.1785/0120140237>
- Jolivet, R., Lasserre, C., Doin, M.-P., Peltzer, G., Avouac, J.-P., Sun, J., & Dailu, R. (2013). Spatio-temporal evolution of aseismic slip along the haiyuan fault, China: Implications for fault frictional properties. *Earth and Planetary Science Letters*, 377, 23–33. <https://doi.org/10.1016/j.epsl.2013.07.020>
- Kapp, P., & Guynn, J. H. (2004). Indian punch rifts tibet. *Geology*, 32(11), 993–996. <https://doi.org/10.1130/g20689.1>
- Kapp, P., Taylor, M., Stockli, D., & Ding, L. (2008). Development of active low-angle normal fault systems during orogenic collapse: Insight from tibet. *Geology*, 36(1), 7–10. <https://doi.org/10.1130/g24054a.1>
- Kapp, P., Yin, A., Harrison, T. M., & Ding, L. (2005). Cretaceous-tertiary shortening, basin development, and volcanism in central tibet. *Geological Society of America Bulletin*, 117(7–8), 865–878. <https://doi.org/10.1130/b25595.1>
- Li, J., & Song, X. (2018). Tearing of indian mantle lithosphere from high-resolution seismic images and its implications for lithosphere coupling in southern tibet. *Proceedings of the National Academy of Sciences*, 115(33), 8296–8300. <https://doi.org/10.1073/pnas.1717258115>
- Li, K., Tapponnier, P., Xu, X., Ren, J., Wang, S., & Zhao, J. (2022). Holocene slip rate along the beng co fault and dextral strike-slip extrusion of central eastern tibet. *Tectonics*, 41(8), e2022TC007230. <https://doi.org/10.1029/2022tc007230>
- Li, K., Xu, X., Tapponnier, P., Kang, W., & Wang, S. (2023). Lake level changes and holocene extension rate across the ns-trending peiku co-gyirong faults, southern tibet. *Tectonics*, 42(5), e2022TC007644. <https://doi.org/10.1029/2022tc007644>

- Liang, S., Gan, W., Shen, C., Xiao, G., Liu, J., Chen, W., et al. (2013). Three-dimensional velocity field of present-day crustal motion of the Tibetan plateau derived from gps measurements. *Journal of Geophysical Research: Solid Earth*, 118(10), 5722–5732. <https://doi.org/10.1002/2013jb010503>
- Maubant, L., Pathier, E., Daout, S., Radiguet, M., Doin, M.-P., Kazachkina, E., et al. (2020). Independent component analysis and parametric approach for source separation in insar time series at regional scale: Application to the 2017–2018 slow slip event in guerrero (Mexico). *Journal of Geophysical Research: Solid Earth*, 125(3), e2019JB018187. <https://doi.org/10.1029/2019jb018187>
- Molnar, P., & Tapponnier, P. (1978). Active tectonics of tibet. *Journal of Geophysical Research*, 83(B11), 5361–5375. <https://doi.org/10.1029/jb083ib11p05361>
- Murphy, M., Sanchez, V., & Taylor, M. (2010). Syncollisional extension along the India–asia suture zone, south-central tibet: Implications for crustal deformation of tibet. *Earth and Planetary Science Letters*, 290(3–4), 233–243. <https://doi.org/10.1016/j.epsl.2009.11.046>
- Ou, Q., Daout, S., Weiss, J., Shen, L., Lazecky, M., Wright, T. J., & Parsons, B. E. (2022). Large-scale interseismic strain mapping of the ne Tibetan plateau from sentinel-1 interferometry. *Journal of Geophysical Research: Solid Earth*, 127(6), e2022JB024176. <https://doi.org/10.1029/2022jb024176>
- Pang, Y., Zhang, H., Shi, Y., & Gerya, T. (2022). Plume-induced rifting of thickened crust: 2d numerical model and implications for n–s rifts in southern tibet. *Geophysical Research Letters*, 49(23), e2022GL101479. <https://doi.org/10.1029/2022gl101479>
- Sanchez, V., Murphy, M., Robinson, A., Lapen, T., & Heizler, M. (2013). Tectonic evolution of the India–asia suture zone since middle eocene time, lopukangri area, south-central tibet. *Journal of Asian Earth Sciences*, 62, 205–220. <https://doi.org/10.1016/j.jseas.2012.09.004>
- Sandwell, D. T., & Wessel, P. (2016). Interpolation of 2-d vector data using constraints from elasticity. *Geophysical Research Letters*, 43(20), 10–703. <https://doi.org/10.1002/2016gl070340>
- Segall, P. (2010). *Earthquake and volcano deformation* (STU - Student edition ed.). Princeton University Press. Retrieved 2024-04-11, from <http://www.jstor.org/stable/j.ctt7sg19>
- Shen, Z.-K., Wang, M., Zeng, Y., & Wang, F. (2015). Optimal interpolation of spatially discretized geodetic data. *Bulletin of the Seismological Society of America*, 105(4), 2117–2127. <https://doi.org/10.1785/0120140247>
- Styron, R. H., Taylor, M. H., Sundell, K. E., Stockli, D. F., Oalmann, J. A., Moeller, A., et al. (2013). Miocene initiation and acceleration of extension in the south lunggar rift, western tibet: Evolution of an active detachment system from structural mapping and (u-th)/he thermochronology. *Tectonics*, 32(4), 880–907. <https://doi.org/10.1002/tect.20053>
- Sundell, K. E., Taylor, M. H., Styron, R. H., Stockli, D. F., Kapp, P., Hager, C., et al. (2013). Evidence for constriction and pliocene acceleration of east-west extension in the north lunggar rift region of west central tibet. *Tectonics*, 32(5), 1454–1479. <https://doi.org/10.1002/tect.20086>
- Tapponnier, P., Mercier, J., Armijo, R., Tonglin, H., & Ji, Z. (1981). Field evidence for active normal faulting in tibet. *Nature*, 294(5840), 410–414. <https://doi.org/10.1038/294410a0>
- Tapponnier, P., & Molnar, P. (1977). Active faulting and tectonics in China. *Journal of Geophysical Research*, 82(20), 2905–2930. <https://doi.org/10.1029/jb082i020p02905>
- Tian, Z., Yang, Z., Bendick, R., Zhao, J., Wang, S., Wu, X., & Shi, Y. (2019). Present-day distribution of deformation around the southern Tibetan plateau revealed by geodetic and seismic observations. *Journal of Asian Earth Sciences*, 171, 321–333. <https://doi.org/10.1016/j.jseas.2018.12.018>
- Wang, H., Wright, T., & Biggs, J. (2009). Interseismic slip rate of the northwestern xianshuihe ltfa from insar data. *Geophysical Research Letters*, 36(3). <https://doi.org/10.1029/2008gl036560>
- Wang, H., Wright, T. J., Liu-Zeng, J., & Peng, L. (2019). Strain rate distribution in south-central tibet from two decades of insar and gps. *Geophysical Research Letters*, 46(10), 5170–5179. <https://doi.org/10.1029/2019gl081916>
- Wang, K., & Fialko, Y. (2018). Observations and modeling of coseismic and postseismic deformation due to the 2015 mw 7.8 gorkha (Nepal) earthquake. *Journal of Geophysical Research: Solid Earth*, 123(1), 761–779. <https://doi.org/10.1002/2017jb014620>
- Wang, M., & Shen, Z.-K. (2020). Present-day crustal deformation of continental China derived from gps and its tectonic implications. *Journal of Geophysical Research: Solid Earth*, 125(2), e2019JB018774. <https://doi.org/10.1029/2019jb018774>
- Wang, Q., Zhang, P.-Z., Freymueller, J. T., Bilham, R., Larson, K. M., Lai, X., et al. (2001). Present-day crustal deformation in China constrained by global positioning system measurements. *Science*, 294(5542), 574–577. <https://doi.org/10.1126/science.1063647>
- Wang, S., Chevalier, M.-L., Pan, J., Bai, M., Li, K., Li, H., & Wang, G. (2020). Quantification of the late quaternary throw rates along the yadong rift, southern tibet. *Tectonophysics*, 790, 228545. <https://doi.org/10.1016/j.tecto.2020.228545>
- Wang, S., Shen, X., Chevalier, M.-L., Replumaz, A., Zheng, Y., Li, H., et al. (2022). Illite k-ar and (u-th)/he low-temperature thermochronology reveal onset timing of yadong-gulu rift in southern Tibetan plateau. *Frontiers in Earth Science*, 10, 993796. <https://doi.org/10.3389/feart.2022.993796>
- Wang, W., Qiao, X., Yang, S., & Wang, D. (2017). Present-day velocity field and block kinematics of Tibetan plateau from gps measurements. *Geophysical Journal International*, 208(2), 1088–1102. <https://doi.org/10.1093/gji/ggw445>
- Wegmüller, U., & Werner, C. (1997). *Gamma sar processor and interferometry software* (pp. 1687–1692). European space agency, (special publication) essa sp. Retrieved from <https://www.scopus.com/inward/record.uri?eid=2-s2.0-5244223739&partnerID=40&md5=1687c7ce58f9c3391546be124f531a4>
- Weiss, J. R., Walters, R. J., Morishita, Y., Wright, T. J., Lazecky, M., Wang, H., et al. (2020). High-resolution surface velocities and strain for anatolia from sentinel-1 insar and gnss data. *Geophysical Research Letters*, 47(17), e2020GL087376. <https://doi.org/10.1029/2020gl087376>
- Werner, C., Wegmüller, U., Strozzi, T., & Wiesmann, A. (2000). Gamma sar and interferometric processing software. *Proceedings of the Ers Envisat Symposium, Gothenburg, Sweden*, 1620, 1620.
- Wolff, R., Hetzel, R., Hölzer, K., Dunkl, I., Xu, Q., Anczkiewicz, A. A., & Li, Z. (2023). Rift propagation in south Tibet controlled by under-thrusting of India: A case study of the tangra yumco graben (south Tibet). *Journal of the Geological Society*, 180(2), jgs2022–090. <https://doi.org/10.1144/jgs2022-090>
- Woodruff Jr, W. H., Horton, B. K., Kapp, P., & Stockli, D. F. (2013). Late cenozoic evolution of the lunggar extensional basin, tibet: Implications for basin growth and exhumation in hinterland plateaus. *Bulletin*, 125(3–4), 343–358. <https://doi.org/10.1130/b30664.1>
- Wright, T., Houseman, G., Fang, J., Maghsoudi, Y., Hooper, A., Elliott, J., et al. (2023). High-resolution geodetic strain rate field reveals internal deformation of Tibetan plateau. *Preprint EarthArXiv*.
- Wu, D.-L., Ge, W.-P., Liu, S.-Z., Yuan, D.-Y., Zhang, B., & Wei, C.-M. (2024). Present-day 3d crustal deformation of the northeastern Tibetan plateau from space geodesy. *Geophysical Research Letters*, 51(4), e2023GL106143. <https://doi.org/10.1029/2023gl106143>
- Wu, Z., Ye, P., Wang, C., Zhang, K., Zhao, H., Zheng, Y., et al. (2015). The relics, ages and significance of prehistoric large earthquakes in the angang graben in south tibet. *Earth Science - Journal of China University of Geosciences*, 40(10), 1621.
- Yin, A., & Harrison, T. M. (2000). Geologic evolution of the himalayan-Tibetan orogen. *Annual Review of Earth and Planetary Sciences*, 28(1), 211–280. <https://doi.org/10.1146/annurev.earth.28.1.211>

- Yu, C., Li, Z., & Penna, N. T. (2018). Interferometric synthetic aperture radar atmospheric correction using a gps-based iterative tropospheric decomposition model. *Remote Sensing of Environment*, 204, 109–121. <https://doi.org/10.1016/j.rse.2017.10.038>
- Zhang, P.-Z., Shen, Z., Wang, M., Gan, W., Bürgmann, R., Molnar, P., et al. (2004). Continuous deformation of the Tibetan plateau from global positioning system data. *Geology*, 32(9), 809–812. <https://doi.org/10.1130/g20554.1>
- Zhang, Y., Heresh, F., & Falk, A. (2019). Small baseline insar time series analysis: Unwrapping error correction and noise reduction. *Computers and Geosciences*, 133, 104331. <https://doi.org/10.1016/j.cageo.2019.104331>
- Zhang, Y., Wimpenny, S., Dal Zilio, L., & Shan, X. (2024). Strain partitioning and fault kinematics in the northern qilian Shan (ne tibet) determined from bayesian inference of geodetic data. *Geophysical Research Letters*, 51(9), e2023GL107324. <https://doi.org/10.1029/2023gl107324>
- Zhao, D., Qu, C., Bürgmann, R., Gong, W., Shan, X., Qiao, X., et al. (2022). Large-scale crustal deformation, slip-rate variation, and strain distribution along the kunlun fault (tibet) from sentinel-1 insar observations (2015–2020). *Journal of Geophysical Research: Solid Earth*, 127(1), e2021JB022892. <https://doi.org/10.1029/2021jb022892>
- Zhonghai, W., Xitao, Z., Zhenhan, W., Wan, J., Daogong, H., & Chunjing, Z. (2004). Quaternary geology and faulting in the damxung-yangbajain basin. *Acta Geologica Sinica-English Edition*, 78(1), 273–282. <https://doi.org/10.1111/j.1755-6724.2004.tb00700.x>
- Zhong-hai, W., Yong-shuang, Z., Dao-gong, H., Xi-tao, Z., & Pei-sheng, Y. (2007). Late cenozoic normal faulting of the qungdo'gyang graben in the central segment of the cona-oiga rift, southeastern tibet (in Chinese). *Journal of Geomechanics*, 13(4), 297–306.